applied sciences

MDPI

Article

Meta-Heuristics Optimization of Mirrors for Gravitational Wave Detectors: Cryogenic Case

Veronica Granata [1,2], Vincenzo Pierro [1,3,*] and Luigi Troiano [1,4]

[1] INFN, Sezione di Napoli, Gruppo Collegato di Salerno, Complesso Universitario di Monte S. Angelo, 80126 Napoli, Italy; vgranata@unisa.it (V.G.); ltroiano@unisa.it (L.T.)
[2] Dipartimento di Fisica "E. R. Caianiello", Universitá di Salerno, 84084 Fisciano, Italy
[3] Dipartimento di Ingegneria, Universitá del Sannio, 82100 Benevento, Italy
[4] Dipartimento di Scienze Aziendali, Management and Innovation Systems (DISA-MIS), Universitá di Salerno, 84084 Fisciano, Italy
* Correspondence: pierro@unisannio.it or vpierro@sa.infn.it

Abstract: In this paper, we explore the behavior of several optimization methods for reducing coating Brownian noise in the mirrors of gravitational wave detectors. We will refer to cryogenic operating temperatures, where the low refractive index material has mechanical losses higher than those of the high refractive index material. This situation is the exact opposite of that which occurs at room temperature, which is already widely known. The optimal design of the dielectric mirror (without a priori assumptions on thicknesses) can be obtained through the combined multi-objective optimization of transmittance and thermal noise. In the following, we apply several multi-objective meta-heuristics to compute the Pareto front related to the optimization problem of dielectric mirror thicknesses made of two materials (binary coatings). This approach gives us more certainty about the structure of the final result. We find strong evidence that all meta-heuristics converge to the same solution. The final result can be interpreted with simple physical considerations, providing useful rules to simplify the thicknesses of the optimization algorithm.

Keywords: coating and dielectric mirrors; gravitational waves detectors; optics

Citation: Granata V.; Pierro V.; Troiano L. Meta-Heuristics Optimization of Mirrors for Gravitational Wave Detectors: Cryogenic Case. *Appl. Sci.* **2022**, *12*, 7680. https://doi.org/10.3390/app12157680

Academic Editor: Salvatore Gallo

Received: 27 June 2022
Accepted: 28 July 2022
Published: 30 July 2022

1. Introduction

The experimental research and the construction of large interferometric ground-based antennas [1–7] aimed at the direct detection of gravitational waves have been very relevant in recent years (see [8,9] for an introduction to the topics). During this period, we have witnessed the first detection of a gravitational wave, as well as the first direct evidence of a black hole mergers [10]; the joint detection achieved with three detectors, which allowed for the great sky localization precision [11] (gravitational astronomy was born); and the the first detection of a multi-messenger event [12,13], the publication of which has ended with the third catalog [14]. To achieve these far-reaching results, there are many problems and technological challenges that researchers have had to overcome, and it is precisely one of these problems that we will discuss below.

In this work, we address the problem of identifying the optimal design of a totally reflective dielectric mirror. The solution to the problem is of particular interest for the realization of gravitational wave detectors [1,5,15,16], which must have the highest possible reflectance and at the same time reduced thermal noise [17,18]. In fact, the sensitivity of gravitational waves detectors is ultimately limited by the various noise sources determining random fluctuations in the physical optical path length, in particular suspension thermal noise and mirror thermal noise.

Therefore, the problem of optimal design naturally presents itself as a multi-objective optimization problem. The highly non-linear and non-convex nature of the reflectance function due to the variation in the length of the layers makes it necessary to use optimization

techniques that do not fall within the canonical methods of mathematical programming [19]. Furthermore, an analytical solution to this problem is not known in the current literature, although solutions very close to the analytical one can be found in the literature [20] for the case of detectors operating at room temperature.

Of course, there are other strategies for noise reduction in gravitational wave coatings: those based on the use of three or more materials [21,22], and the production of nano-engineered materials [23]. In this area, the study of the crystallization of materials as a function of deposited thickness becomes crucial [24].

In this paper, we address the problem using a meta-heuristic approach. In particular, we ask whether there is a single criterion (i.e., independent of the optimization method used) that is representative of the set of solutions that make up the Pareto front.

In other words, the objective of the paper, rather than focusing on a specific optimization technique, is to answer the question of whether there is also a unique criterion of optimal design in the case of cryogenic detectors, and of what its physical interpretation is. To achieve this goal, we compare the solutions offered by a multiplicity of multi-objective meta-heuristic optimization methods with constraints. We will select among multiple optimization methods those that have demonstrated well-established validity in applications. Furthermore, the solution found offers some non-trivial physical interpretation cues and original design criteria, showing a performance limit.

The remainder of this paper is organized as follows: Section 2 illustrates the physical model of the dielectric mirror in the context of gravitational wave detection; Section 3 illustrates the mathematical formulation of the optimization problem; Section 4 outlines the methods employed for solving the optimization problem; Section 5 reports the experimental findings, describing the physical meaning of results; and the conclusions and perspective are discussed in Section 6.

2. The Physical Model

In this section, we start describing the electromagnetic model of a coating made of dielectric layers. This device is designed to reproduce the behaviour of a low-absorption perfect mirror, i.e., of a mirror with a reflection coefficient near to the unity. The electromagnetic behaviour of a coating can be obtained by a simple matrix method [25] (for a comprehensive introduction to the topic of layered structures, see [26,27]). The optical response of a coating can be computed from the multi-layer characteristic matrix,

$$\mathcal{T} = \mathcal{T}_1 \cdot \cdots \cdot \mathcal{T}_m \cdot \cdots \cdot \mathcal{T}_{N_L} \tag{1}$$

where N_L is the total number of layers numbered from the vacuum to the substrate, as illustrated in Figure 1. The matrix $\mathcal{T}_m$ is associated with the geometrical and material properties of the layer

$$\mathcal{T}_m = \begin{bmatrix} \cos(\xi_m) & \imath (n^{(m)})^{-1} \sin(\xi_m) \\ \imath n^{(m)} \sin(\xi_m) & \cos(\xi_m) \end{bmatrix}, \tag{2}$$

where in the case of normal incidence

$$\xi_m = \frac{2\pi}{\lambda_0} n^{(m)} z_m. \tag{3}$$

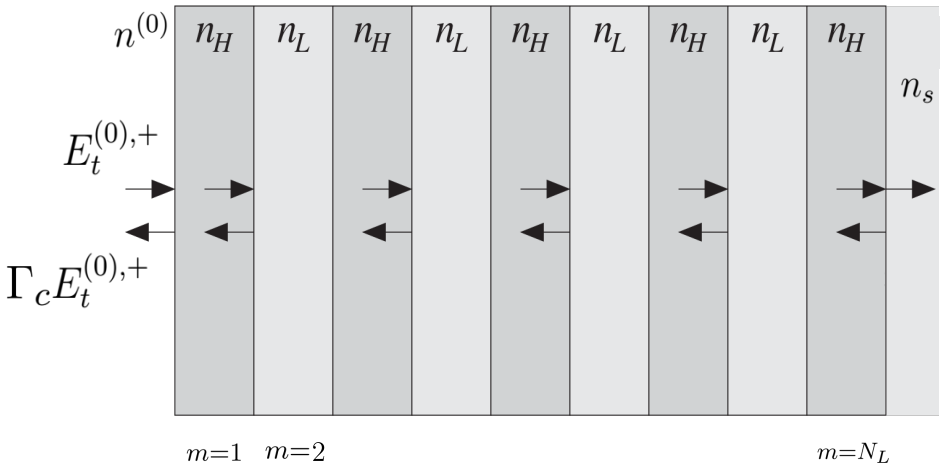

Figure 1. The figure shows the sketch of a multilayer structure with an electromagnetic wave coming from the left, i.e., a monochromatic plane wave; an exp $\iota\omega t$ dependence on time is supposed, and λ_0 is the free space wavelength. The symbol Γ_c denotes the complex reflection coefficients, while n_H and n_L are the refractive indices of the alternating layers. The parameters of the densest material have the subscript H, shile those of the least dense material have the subscript L. The indices $n^{(0)}$ and n_s are the refractive indices of the vacuum and substrate, respectively.

We have defined λ_0 and z_m as the free space wavelength (i.e., the laser frequency) and the layer thickness, respectively, and $n^{(m)}$ is the refractive index of the m-th layer. The refractive index of the whole coating can be obtained by using n_l, i.e., the refractive index of the layered structure:

$$n_l = \frac{\mathcal{T}_{21} + n_s \mathcal{T}_{22}}{\mathcal{T}_{11} + n_s \mathcal{T}_{12}}, \tag{4}$$

where n_s is the refractive index of substrate (see Figure 1) and $\mathcal{T}_{ij}$ represents the components of characteristic Matrix (2). The Formula (4) can be used to compute the power transmittance τ_c at the vacuum/coating interface :

$$\tau_c = 1 - \left| \frac{n^{(0)} - n_l}{n^{(0)} + n_l} \right|^2. \tag{5}$$

where $n^{(0)} = 1$ is the refractive index of the vacuum. In the following, we should minimize the transmittance τ_c as a function of $\bar{z}_m = z_m/\lambda_0$, the normalized layer thicknesses. The reduction of transmittance is a general problem of the optical design of dielectric layered structures, and the peculiarity of the gravitational wave coating design problem consists of obtaining such a minimum constraint on the thermal noise .

Thermal noise in the coatings of the test-masses is presently the dominant noise source in interferometric gravitatinal wave detectors [17], their ultimate visibility distance is set in the (40–300) Hz band. The power spectral density of coating thermal noise is given, under suitable simplifying assumptions, by [28]

$$S^B_{coat} = \frac{2k_B T}{f\pi^{3/2}} \frac{1 - \sigma_s^2}{w Y_s} \phi_c \tag{6}$$

where f is the frequency; T is the (absolute) temperature; w is the (assumed Gaussian) laser-beam waist; and σ_s and Y_s are the Poisson and Young modulus of the substrate, and the coating loss angle ϕ_c. It is clear from Equation (6) that a viable method of reducing thermal noise is to lower the temperature down to cryogenic values (i.e., $T \sim 20$ K). The use of cryogenic techniques to reduce the thermal noise of the coating, unfortunately, is limited by the phenomenon of cryogenic peak of silica [29]. In particular, the mechanical losses of silica

(the low-contrast material) worsen significantly at very low temperatures. The optimization technique developed in this paper attempts to reduce the worsening of the loss angle due to this cryogenic peak phenomenon. In this connection, we introduce a functional producing the thermal noise of coating as a function of the normalized thicknesses of the layers

$$\phi_c = \sum_{m=1}^{N_L} \eta_m \bar{z}_m \tag{7}$$

where η_m are the specific thermal noise coefficients depending on the material that constitutes the layer. The noise model used here is the one described in [28]; other models are available in the literature [30], but despite their supposed higher accuracy they provide comparable results (see discussion in [31] and supplementary material therein).

In the following, we study the dielectric structure made of alternating layers of two materials indicated with the subscripts H and L, with the refractive index n_H and n_L, and specific normalized loss coefficient η_H and η_L. The type L material is a low refractive index material; thus, we have by definition $n_L < n_H$.

In view of the linearity of ϕ_c functional, see Equation (7), both as a function of $\bar{z}_m$ and η_m, we can take as a reference the material H and pose $\eta_H = 1$. This normalization takes the lower specific noise coefficient between the two materials as unitary; in the cryogenic case (due to the cryogenic peak of L-type material), the H-type material (supposed to have lower mechanical losses) is taken as a reference (at room temperature the situation is reversed).

Considering the above definitions and for a dielectric mirror made of two alternating materials starting with the H layer, we have the following functional:

$$\phi_c = \sum_{m=0}^{\lfloor N_L/2 \rfloor} \bar{z}_{2m+1} + \sum_{m=1}^{\lfloor N_L/2 \rfloor} \eta_L \bar{z}_{2m} \tag{8}$$

in this case, we should suppose that N_L is an odd number, in order to have an H-type layer at the end of the device. The opposite case, where the first layer is an L-type material, leads to the following formula:

$$\phi_c = \sum_{m=1}^{\lfloor N_L/2 \rfloor} \eta_L \bar{z}_{2m-1} + \sum_{m=1}^{\lfloor N_L/2 \rfloor} \bar{z}_{2m}. \tag{9}$$

where N_L is supposed even in order to terminate the device with an H-type layer. The last layer is, in any case, the high refractive material in the sense that the substrate has a refractive index such that $n_s \sim n_L$ (i.e., low contrast).

3. The Optimization: The Mathematical Problem

In this section, we formulate, in three different ways, the optimization problem for coatings used as high reflective mirros in gravitational wave detectors. The problem formulation applies to both cases of sequences beginning with either material L or material H; obviously, the transmittance and noise functionals must change according to the sequences.

First of all, the search space Ω is defined by the following inequalities: $0 \leq \bar{z}_m \leq 0.5/n_H$ for m where $n^{(m)} = n_H$ (H-type layers), and $0 \leq \bar{z}_m \leq 0.5/n_L$ for m where $n^{(m)} = n_L$ (L-type layers). The straightforward definition of the optimization problem, driven by physical interpretation, is

$$\begin{aligned} &\underset{\bar{z}_1,\ldots,\bar{z}_{N_L} \in \Omega}{\text{Min}} && \phi_c(\bar{z}_1, \ldots, \bar{z}_{N_L}). \\ &\text{subject to} && \tau_c(\bar{z}_1, \ldots, \bar{z}_{N_L}) \leq \tau_0 \end{aligned} \tag{10}$$

The problem in (10) can be alternatively written [32]:

$$\begin{aligned} \underset{\bar{z}_1,\ldots,\bar{z}_{N_L}\in\Omega}{\text{Min}} \quad & \tau_c(\bar{z}_1,\ldots,\bar{z}_{N_L}) \\ \text{subject to} \quad & \phi_c(\bar{z}_1,\ldots,\bar{z}_{N_L}) \leq \phi_0 \end{aligned} \tag{11}$$

where ϕ_0 is the maximum allowed loss angle and τ_0 is the constraint on the transmittance. In the paper [33], it has been shown that the constrained optimization problems (10) or (11) can be further formulated in an equivalent multi-objective fashion, as follows:

$$\underset{\bar{z}_1,\ldots,\bar{z}_{N_L}\in\Omega}{\text{Min}} \quad [\phi_c(\bar{z}_1,\ldots,\bar{z}_{N_L}), \tau_c(\bar{z}_1,\ldots,\bar{z}_{N_L})]. \tag{12}$$

The coating optimization using the multi-objective approach reduces to the computation of the Pareto front of the optimization problem (12); for a tutorial on multi-objective optimization, see [34]. In [33], it has been shown that the three formulations of the optimization problem (10)–(12) are equivalent, for the case of coatings designed to operate at room temperature. It must be remembered that the problem (10) can be solved using the Pareto front of (12), by choosing the point on the Pareto boundary with a transmittance component equal to τ_0. Similar considerations can be made for the problem (11), which can be solved by taking the point on the Pareto boundary with a noise component equal to ϕ_0. Such a result arises from the properties of the Pareto front, which turns out to be continuous and monotonic for the problem (12). In the remainder of this paper, we will show that the above results are also true in the case of the optimization of coatings operating at cryogenic temperatures.

4. The Optimization Methods

The problem of optimized coating can be tackled using a series of algorithms that, over the years, have been developed specifically for multi-objective optimization problems. In our experimentation, we compared the following algorithms: NSGA2, NSGA3, GDE3, MOEA/D, Borg MOEA, and Particle Swarm (MOPSO). In the following subsections, we will describe the heuristic optimization algorithms used in the simulations. This paragraph does not seek to describe in detail all the methods but only to supply one road map for the reader who wants to explore this matter further.

4.1. Optimization Heuristic NSGA2 and NSGA3

The NSGA2 algorithm (see references [34,35]) implements two main strategies: a fast non-dominated sorting solution, and the preservation of the solution's diversity. The initial population is generated at random according to the number of defined chromosomes. The population sorting is made by non-dominated solutions. This step follows the same procedure used in [35]; the crowding distance is also applied. The selection (i.e., the natural selection) is made by the tournament method, where the confrontation of two individuals of the initial population (chose at random) is made to stock the individuals with the best Pareto front. If the two confronted members are of the same front, the decision is made according to the crowding distance criteria. The crossover algorithm generates two cut-points selected at random in one parent, so the chromosome is divided into three sub-vectors (segments); then, the first segment is exchanged with the last one.

The last step is a population update. After applying the genetic operators and the population sorting criterion (fronts and crowding distance), we must determine the individuals that will be kept for the next generation. We begin with an initial population; we create the children in order to have a final population that will be classified in terms of fronts and the crowding distance to keep a constant number of individuals (i.e., the population size remains unchanged).

The NSGA3 algorithm is a modification of NSGA2 specifically designed to handle optimizations with more than two objectives. This enhanced algorithm was proposed in [36] but with some selection mechanisms changed.

4.2. Optimization Heuristic GDE3

Generalized differential evolution (GDE3) is an algorithm that extends differential evolution in order to tackle multi-objective optimization problems [37] with an arbitrary number of objectives and constraints. The differential evolution [38] optimizes a problem by maintaining a population of candidate solutions and creating new candidate solutions by combining existing ones according to simple (linear) formulae. The candidates with the best fitness with respect to the optimization problem at hand are introduced into the population. In this way, the optimization problem is treated as a black box that merely provides a measure of the fitness of the candidates in the population (the gradient is therefore not needed).

4.3. Optimization Heuristic MOEA/D

The MOEA/D is a multi-objective evolutionary algorithm based on decomposition. This method is a general-purpose algorithm framework; it decomposes a multi-objective optimization problem into a number of single-objective optimization sub-problems (or simple multi-objective optimization problems) and then uses a search heuristic to optimize these sub-problems simultaneously and cooperatively (see the seminal paper [39]; for recent developments, see [40]).

4.4. Optimization Heuristic Borg MOEA

To solve optimization problems with an evolutionary algorithm, the individuals of a population are associated by the encoding procedure to a physical solution of a given problem (in our case, the layer thicknesses sequence); the selection probability is proportional to the quality of the represented solution, i.e., to the fitness function to be optimized.

The population then undergoes selection crossover and mutation (like in natural genetics evolution), producing new children and updating the population [41]. The process is repeated over various generations until a suitable termination criteria is reached.

The peculiarity of the Borg MOEA evolutionary method consists in changing the above-described operators adaptively [42,43]. The Borg MOEA algorithm is therefore more robust with respect to the probability of being trapped in local minima. Let us emphasize that among all the algorithms used in this paper, Borg MOEA has already been successfully applied to the coating optimization problem in Ref. [33] in the case of mirrors operating at room temeprature.

4.5. Optimization Heuristic Particle Swarming (MOPSO)

The particle swarm optimization is a heuristic method that optimizes a problem by iteratively trying to improve a candidate solution with regard to a given measure of quality (fitness function), possibly subject to a constriant (see the seminal paper [44,45]). It solves a problem by having a population of candidate solutions, here dubbed particles, and moving these particles around in the search space according to a simple mathematical formula for the particle's position and velocity. Each particle's movement is influenced by its local best known position but is also guided toward the best known positions in the search space, which are updated as better positions are found by other particles. This is expected to move the swarm toward the best solutions. For an updated account of the method, including also the multi-objective variant, we refer to [46] and references therein.

5. Numerical Experiments

We perform many numerical experiments with different meta-heuristics to obtain strong evidence that the Pareto front and its properties of continuity and monotony are

confirmed, and that all methods converge to the same endpoint. As mentioned above, in a previous paper [33] clear indications of the structure and convergence of Pareto fronts and design were found using only the Borg MOEA meta-heuristic [43], in the case of the room temperature operation of the coating.

In this paper, we generalize the numerical experiments by implementing different algorithms and considering a physical situation that was never analyzed previously. The behavior at room temperature ($T = 300$ K) of the dielectric mirror was found by using for H and L-type materials the values $\eta_L = 1$ and $\eta_H \sim 10$; at cryogenic temperature ($T = 20$ K), the situation could be reversed, i.e., $\eta_L \sim 10$ and $\eta_H = 1$.

In the following, we will focus on the optimization of coatings based on layer sequences starting with material H because it has been observed that the optimization of sequences starting with material L always reduces to the latter.

Assuming that the relationship between the specific noise coefficients is $\eta_L > \eta_H$ (in particular, $\eta_L \sim 10$ and $\eta_H = 1$), we perform simulations with the following algorithms: GDE3, NSGA2, NSGA3, MOEA/D, Borg MOEA, and MOPSO, to verify that the results found in [33] remain valid (see [47,48] for pratical implementations of considered heuristics).

We find that each of the previous heuristics converges with its specificity toward a common trade-off curve. Finally, the result can be interpreted with physical considerations, providing useful rules to simplify the design structure on which to perform thickness optimization.

5.1. Asseveration of Convergence

In order to better describe the results of the convergence of the various optimization methods used, we introduce the common Pareto Front. This common Pareto front is obtained by combining (i.e., joining together) the lists of the different Pareto fronts found with the methods indicated above and extracting a single Pareto front made of all the non-dominated points [49]. In Figure 2, we show the common Pareto front for the above methods; the parameters used in the simulations are reported in the caption of the figure itself (the same as the end of Table 1); the number of the layers is $N_L = 23$, and the red dot shows the position of the quarter wavelength design (which terminates the tradeoff curve).

Table 1. Physical parameters of the H- and L-type materials, used in the simulations at cryogenic temperature (we suppose that the laser operating wavelength is $\lambda_0 = 1550$ nm). The substrate has the same refractive index as the L-type material $n_s = n_L$.

Property	***H* Material**	***L* Material**
refractive index	2.1	1.45
loss angle	10^{-4}	7.8×10^{-4}
extinction	4×10^{-8}	8.4×10^{-11}
η coeff.	1	7

Some interesting comments have already been made on Figure 2; even in the case of cryogenic temperature (where the parameters fulfill the relation $\eta_H < \eta_L$), the Pareto front has several bumps (see closeup in Figure 2) and is therefore not convex. Compared to the case studied in the literature by some of us (i.e., $\eta_H > \eta_L$), a discontinuity appears in the closeup region. This discontinuity present at high transmittance arises from the abrupt transition in the optimal mirror design that occurs when going from one layer of the H-material to two layers of the H and L materials (in the cryogenic case it has a highly specific noise coefficient).

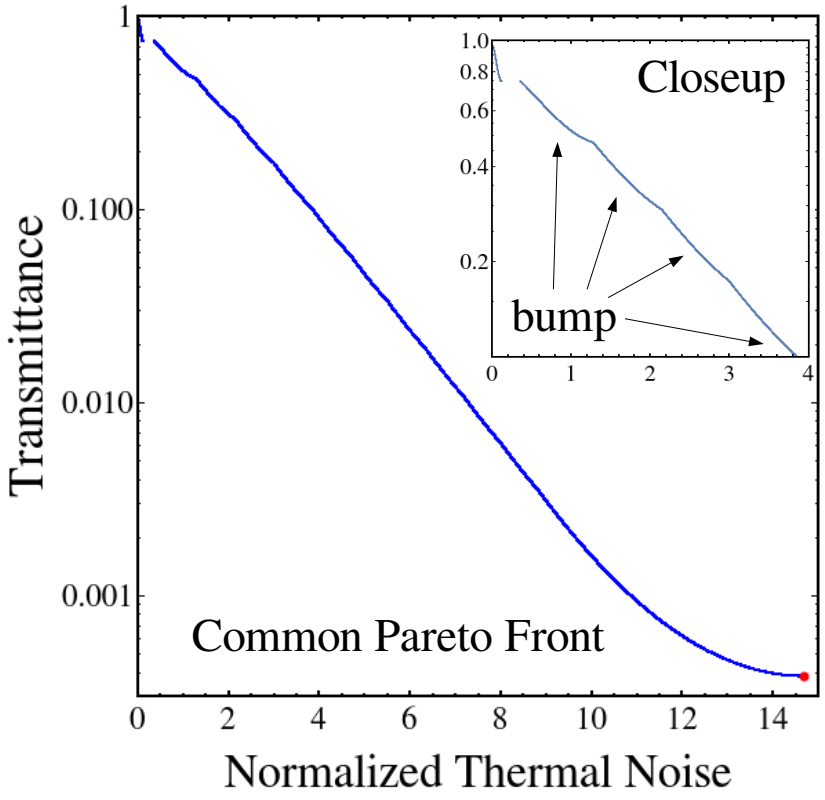

Figure 2. The figure shows the common Pareto Front for the GDE3, NSGA2, NSGA3, MOEA/D, Borg MOEA, and MOPSO methods. The execution time of each method is 10^5 s; the parameters used in the simulation are reported in Table 1, and $N_L = 23$ is the total number of alternating layers. The red dot represents the performance of the quarter wavelength coating with $N_L = 23$ layers. At the top right of the figure, a closeup of the region with high transmittance and low thermal noise is shown. It is clear that the Pareto front is bumpy and therefore not convex; it shows a discontinuity in the closeup region.

In Figure 3, the absolute errors of the various trade off curves with respect to the common Pareto front, each computed with its algorithm, are shown. The vertical green line shows the last point computed by the heuristics, indicating the termination of the numerical Pareto curve. This line is not shown when it coincides with the quarter wavelength coating design (the endpoint of the Pareto front, the red dot in Figure 2). Note the empty spaces (see the dashed light blue area) in the panel of the Borg MOEA and MOEA/D methods, before the last point on the Pareto curve. In that range, the absolute error is comparable to numerical accuracy, which is why it was not reported. The tendency of the Pareto fronts to concentrate on a region of the constraint space (often called focus in the jargon) is one of the methodological problems studied in the literature [50]. In some recent papers on the subject, some authors have stated that they can exploit this tendency to reduce the computational load and speed up the convergence to a specific region of constraint space of greater interest [51].

For the heuristics in Figure 3 indicated with NSGA2 and NSGA3 labels, we show, in red, the error curves of the methods when the evolution time is halved. These curves give us quantitative information about error reduction and confirm that the optimization methods converge. Similar curves have been computed for all algorithms (although not reported) showing the same direction of error reduction. In the panels related to MOEA/D and GDE3, we show, in red, the error curves for the Pareto fronts computed, adding a further constraint on the transmittance (i.e., $\tau_c < 0.01$) and leaving the computation time unchanged. With this expedient, we see that is possible to slightly improve the performance of these two methods in the low transmittance (high thermal noise) region. The improvement of the

convergence of these two methods is also shown in Figure 4, where the three trade-off curves for the MOEA/D and GDE3 methods are shown. In this figure, the yellow curve is the common trade-off curve, and the red and green curves are the Pareto front with and without the additional constraint, respectively.

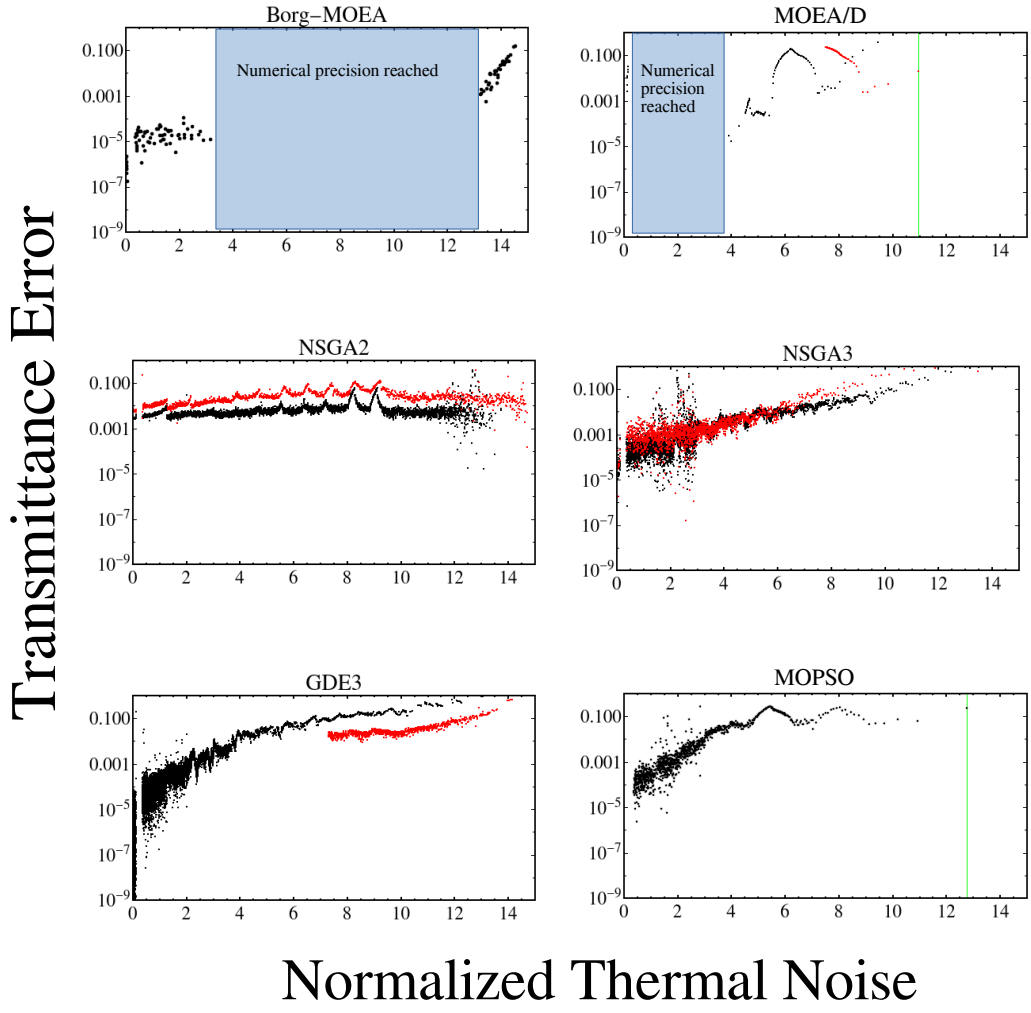

Figure 3. The figure shows the absolute errors of the individual Pareto fronts compared to the common Pareto front. The parameters of the materials are reported in Table 1, and the coating designs are the same as those displayed in Figure 2. In the panels, the green vertical bar (if present) indicates the last point computed by the used heuristics and placed on the numeric Pareto front. The light blue area indicates the region where absolute error is comparable with numerical precision. The execution time is 10^5 s and is the same for all the simulations. For the panels relating to NSGA2 and NSGA3, we show, in red, the error curves of the methods when the evolution time is halved. In the panels labeled MOEA/D and GDE3, we show, in red, the error curves for the Pareto fronts constrained to stay in the low transmittance region (less than $\tau_c < 0.01$); also, in this case, the computation time is 10^5 s and the physical parameters are unchanged.

Let us now comment on the set of Figures 2–4; it is clear that regardless of the heuristics used, there is a unique convergence towards a well defined Pareto front. This is, in our opinion, the main result of this work. It can be seen that each method converges with its peculiarities. Some heuristics converge well across the accessible noise range before quarter-wave design (NSGA2, Borg MOEA); others focus more (GDE3, NSGA3, and MOPSO) or less (MOEA/D) well on the part with low noise and high transmittances. The peculiarities found are well known in the literature [34], and therefore we will not dwell on them later.

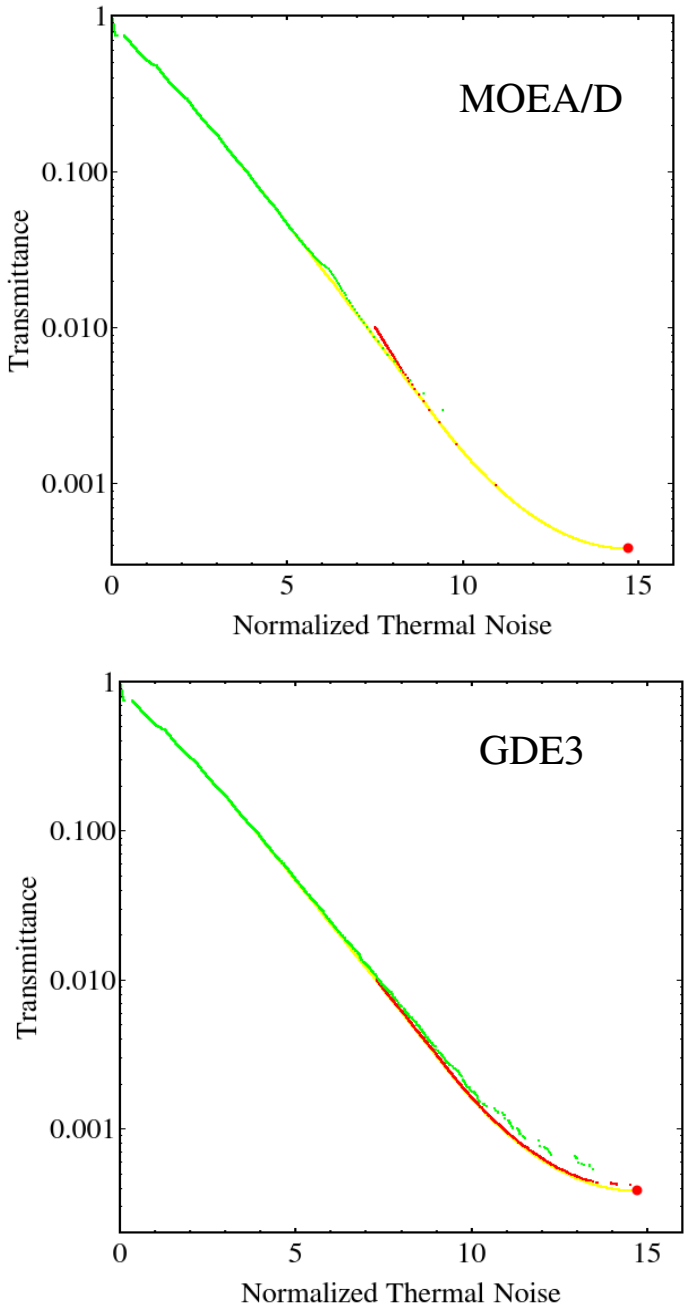

Figure 4. The figure shows the common Pareto Front (yellow) and the two curves computed with and without the constraint on the transmittance, for the two optimization procedures MOEA/D and GDE3. A fortiori, it can be seen that without constraint on transmittance, the two heuristics poorly reconstruct the low-transmittance part of the trade-off curve (the green curve). The red curve shows the Pareto curve with the constraint to look for solutions below the transmittance values of $\tau_c < 0.01$. The computation time is 10^5 s, and the physical parameters are reported in Table 1.

5.2. Physical Properties of the Optimal Design

In this section, we try to understand what happens to the common Pareto fronts when the number of layers of the two materials used is increased. This comparison is made in Figure 5, where using the same parameters of Table 1, different Pareto fronts, obtained by changing the number of layers, are shown. The analysis of Figure 5 reveals that common Pareto fronts tend to collapse on a single asymptotic (bumpy) curve. It has been verified that for the realisitc values of N_H (i.e., $\sim$20), this asymptotic Pareto front is near a decreasing exponential, i.e., the gray dashed line shown in Figure 5. This behavior is the analog of

that found in [33] and further elucidated in [20]; the gray dashed line in Figure 5 is the perfomance limit of the optimization method. The equation of the decreasing exponential in the cryogenic case becomes

$$\log(\tau_c) = \log\left(\frac{4}{n_L}\right) - \frac{2n_H\eta_e}{\eta_e n_H + n_L}\log\left(\frac{n_H}{n_L}\right) + \\ - \bar{\phi}_c \frac{8n_L n_H}{\eta_e n_H + n_L}\log\left(\frac{n_H}{n_L}\right) \tag{13}$$

where τ_c is the trasmittance, ϕ_c is the normalized thermal noise, and $\eta_e \sim 6$ is the effective noise ratio (the value is relevant for the materials considered in Table 1). The result (13) is obtained by specializing the reasoning made in the Appendix of paper [33] to the cryogenic case. The asymptotic curve (13) is dominated by the red straight line in Figure 5, which represents the curve on which the quarter-wave designs are located. Figures 3 and 5 suggest that the number of bumps present on the Pareto Front is equal to the number N_H of layers made of the H-type material. Let us recall that for designs starting with an H-type material at the interface with the vacuum, the following relationship applies $N_L = 2N_H - 1$.

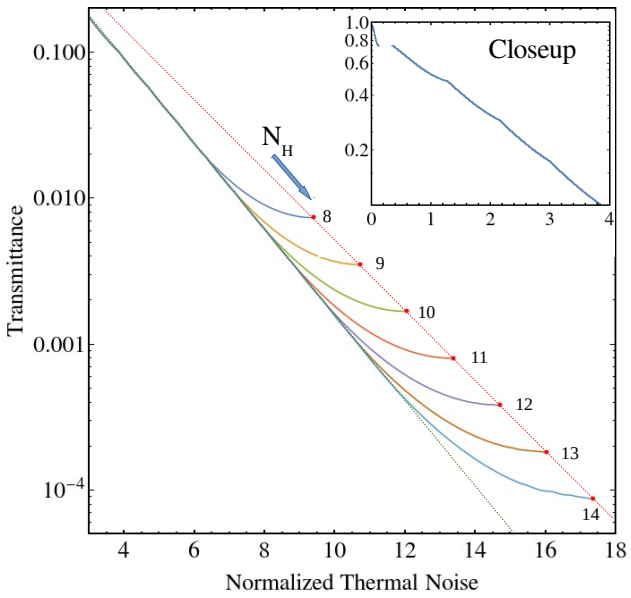

Figure 5. Various common Pareto fronts for $N_H = 8\,(1)\,14$ are shown in the figure. It can be seen that the common Pareto fronts join together in a single curve in the region with high transmittances and low noise. The bump-like structure is also present here; the number of bumps is equal to the number of layers with a high refractive index N_H. The gray dashed line in the figure represents the curve in Equation (13) to which the Pareto fronts approach when N_H increases. The physical parameters are those of Table 1, and the common Pareto fronts are computed by implementing the above-mentioned meta-heuristics each running for 10^5 s.

In the previous section, we have seen that the common Pareto front has bumps. In this section, we will try to explain where they come from. To this end, recall that the trade-off curves shown above were obtained by considering that the thicknesses of all the layers may vary without a priori assumptions.

Let us now introduce the trade-off curves for the periodic structures, i.e., the periodic designs in the thicknesses and in the materials. The periodicity assumption reduces the optimization problem to the maximization of a function of two variables with a linear constraint (see Refs. [32,52] for the development of this idea). The thicknesses of the two alternating materials are the unknowns to be optimized; the number of periodic doublets is to be considered as a parameter. Additionally, in this simple case, we can identify a Pareto

curve that varies with the number of doublets, i.e., it varies with the number of H-type layers. It is necessary to take a small precaution for the design that, at the first interface (near to the vacuum), has an H-type material layer; the last L-type layer should not be taken into account in the noise computation, being of the same material as the substrate (in principle it can be removed without affecting the coating transmittance). With these considerations in mind, we comment on Figure 6, where the common Pareto front for $N_H = 12$ (i.e., $N_L = 23$) is shown together with the Pareto fronts of the periodic design; the numbers of H-type layers change accordingly $N_H = 3(1)8$. The envelope of the periodic case Pareto fronts always lies above the common Pareto front. Furthermore, in Figure 6 it is noted that each bump of the common Pareto front is close to a periodic design Pareto front with given N_H. This is further elucidated in Figure 7; in the upper right b) panel we display the closeup of two common Pareto fronts with $N_H = 12$, 14 (they join together, as noted before). In the same panel, the periodic design Pareto fronts for $N_H = 3$, 4, 5, are displayed and all the curves of the Pareto fronts are intersected with a horizontal straight line, indicating a transmittance of $\tau_c = 0.2$. The intersection identifies a point on (both) the common Pareto fronts that is in the fourth bump (counting from above). Furthermore, the line $\tau_c = 0.2$ intersects the periodic design Pareto curve with $N_H = 4$ i.e., the curve with four H-type layers. In the upper left panel (a) this periodic design is shown, and in the same column in the panels (c) and (e), the design relative to the common Pareto fronts with $N_H = 12$, 14 is shown. The periodic design for $\tau_c = 0.2$ in panel (a) does not seem to be similar to those obtained from the common Pareto fronts in panels (c) and (e), but if we manipulate the thicknesses sequence by eliminating layers with thicknesses much smaller than $\lambda/4$ and joining two contiguous layers of the same material, then the situation changes. This reduction was performed on the sequences displayed in (c) and (e) by providing panels (d) and (f); it is clear that the two solutions are very similar to panel a), and all three correspond to a quasi-periodic design with initial and final tweaking.

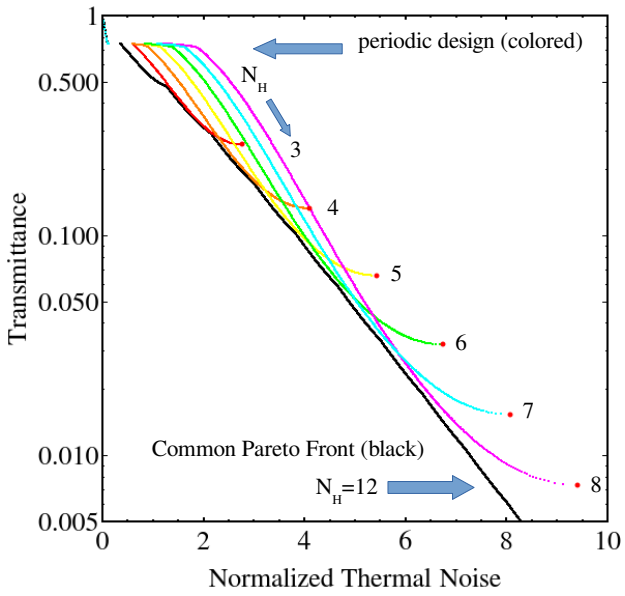

Figure 6. The common Pareto fronts for $N_H = 12$ are shown in the figure; furthermore, in the figure we show the Pareto fronts for periodic designs with the variable $N_H = 3(1)8$. The envelope of the periodic Pareto fronts always lies above the common Pareto front. The physical parameters are those of Table 1, and the common Pareto front is computed by implementing the above-mentioned meta-heuristics, with each running for 10^5 s. The Pareto tradeoff curves of the periodic design are computed in $\sim 10^2$ s.

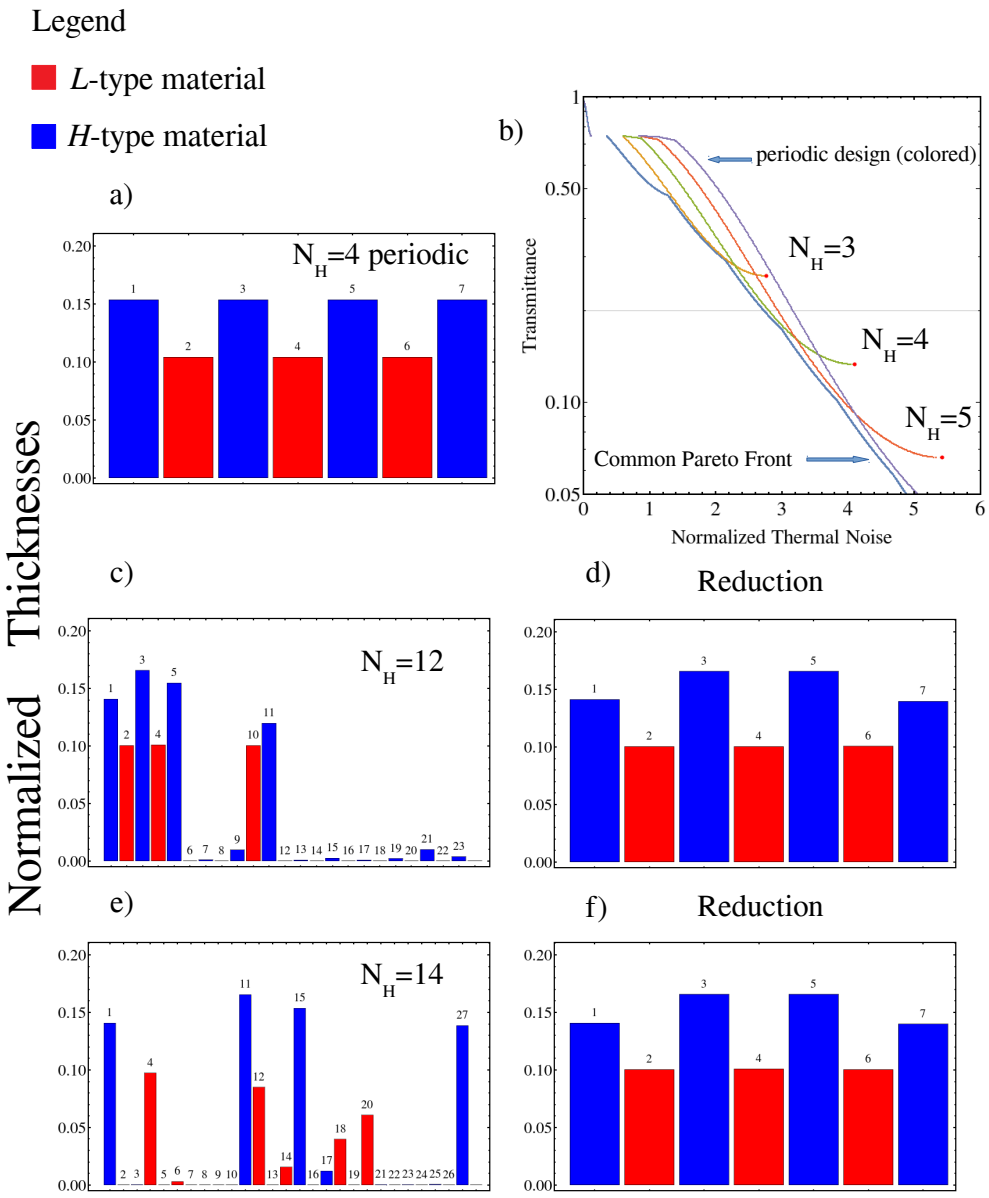

Figure 7. In the panel (**b**), we show the common Pareto fronts for $N_H = 12, 14$ (see arrow in the figure), and the Pareto curves for $N_H = 3$, 4, and 5 in the case of periodic design . Panel (**a**) shows the periodic design (i.e., the thicknesses sequence) in the case $N_H = 4$; this design correspond to the point on the Pareto front (the green line in panel b) with $\tau_c = 0.2$. In panels (**c**,**e**), the computed optimal design for $\tau_c = 0.2$ on the common Pareto fronts are displayed; on the right in panels (**d**,**f**), we see the corresponding design after the reduction operation. In panels (**a**,**c**,**e**,**f**), the blu bar (resp. red) corresponds to the *H*-type material (resp. *L*-type). The physical parameters are those of Table 1, and the common Pareto front is computed by implementing the above-mentioned meta-heuristics, with each running for 10^5 s.

5.3. The Coating Length Optimization

In this section, we shall carry out some recapitulation. In previous articles [32,52], we studied coating optimization in the case of two materials at room temperature, assuming that the pattern structure was periodic, leaving open the possibility of alternative designs (completely aperiodic). The first suggestion that quasi-periodic structures (i.e., periodic

structures with thicknesses tweaked in the top and bottom layers) with two materials could be the only solution is formulated in [33]. In this paper, we show the uniqueness of the convergence by analyzing many optimization methods in the case of two materials at cryogenic temperatures (i.e., $\eta_H < \eta_L$).

We find strong evidence that tweaked periodic designs are the optimized designs; no other possible designs are allowed, as in the case of purely mathematical interest $\eta_H = \eta_L = 1$ (the case of minimal coating length). This is shown in Figure 8, where for $N_H = 10$ we display the common Pareto front in the panel (a). We note that for this case, the monotonic properties of the Pareto front are preserved, but discontinuities appear near the red dots representing the quarter-wave designs.

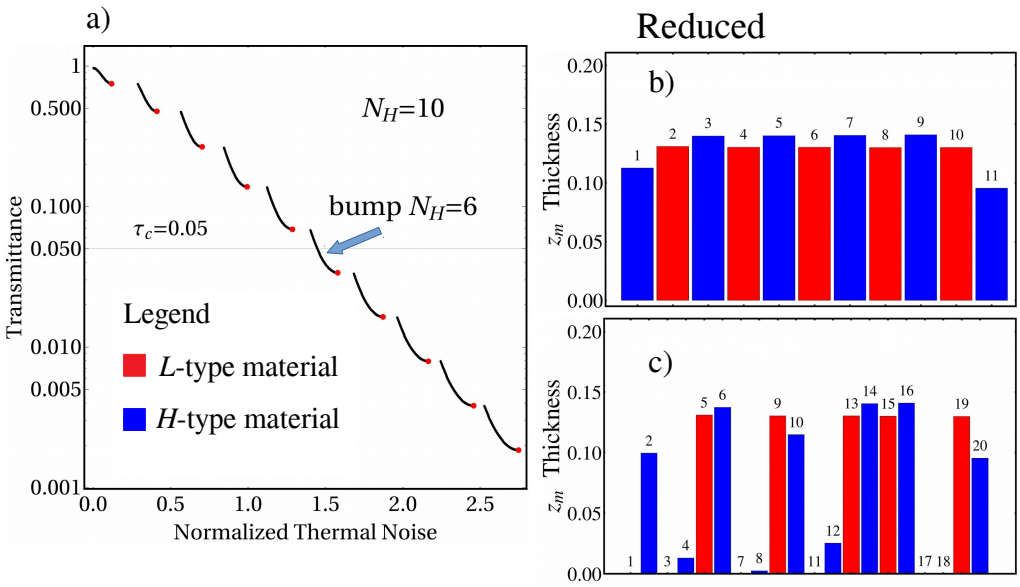

Figure 8. The panel (**a**) of the figure shows the common Pareto front in the case $\eta_H = \eta_L = 1$; the dielectric parameters are the same as in Table 1. The red dots represent the $\lambda/4$ design. For the case $\tau_c = 0.05$ in the right panel (**c**), the corresponding design is shown, and in the above panel (**b**), the reduced design is shown. In the panels (**b**,**c**), the blue bar (resp. red) corresponds to H-type material (resp. L-type). The common Pareto front is computed by implementing the above-mentioned meta-heuristics, with each running for 10^5 s.

To show that the similar conclusions discussed above on the tweaked design also hold true in this case, we add panels (b) and (c) in Figure 8. In these two panels of Figure 8, the design for $\tau_c = 0.05$ on the common Pareto fronts in panel (b) and the reduced design (with $N_H = 6$) are displayed, showing that the tweaked quasi-periodic structure is again the best configuration of the layer thicknesses.

6. Conclusions

This work conclusively addresses a problem of great importance in the construction of gravitational wave antennas. The problem of optimizing the dielectric mirrors of the Fabry–Perot constitutes one of the arms of the Michelson–Morley interferometer. The aforementioned problem, in our opinion, also has relevance for the optics since this research field is new and full of possible applications. Normally, in the theory and practice of multilayer coatings in optics, the focus is on optimizing reflectance alone. The coating-design optimization problem for dielectric mirrors of gravitational wave antennas is an inherently multi-objective problem that we propose to address with appropriate global optimization heuristics. In this connection, we propose to simultaneously minimize the transmittance and the thermal noise of the mirrors.

In a previous paper [33], we analyzed the case of global multi-objective optimization of a coating operating at room temperature, where the relation $\eta_H > \eta_L$ holds. In [33],

however, a thorough convergence analysis has never been done, using only an optimization method (i.e., BorgMOEA). Unfortunately, when using heuristic global optimization methods, for nonlinear and nonconvex problems, there is always the possibility that they will be trapped in local minima by not converging to the sought solution.

In this work, we extend the study to the cryogenic case $\eta_H < \eta_L$, and for completeness to the case of purely mathematical interest $\eta_H = \eta_L$ (coating length minimization). We find that in all physically relevant cases, the global multi-objective optimization heuristics (GDE3, NSGA2, NSGA3, MOEA/D, Borg MOEA, and MOPSO) converge to the same trade-off curves, and all features of the Pareto fronts and the optimal designs shown in [20,33] hold regardless of the global optimization method used. This is the first strong evidence of the correctness and uniqueness of the optimal designs previously found and is also the main result of this paper. The optimal design found, i.e., the sequence of the layers thicknesses of the dielectric mirrors, falls in all cases in the class of tweaked periodic structures. These structures improve the performance of the periodic designs analyzed in Refs. [32,52], which are therefore sub-optimal. Furthermore, it is definitively excluded that other types of designs, i.e., fractal or aperiodic, can improve the performance of the dielectric mirror. In fact, we have verified that the heuristics used in the present work to compute Pareto fronts and optimal designs, when applied to the room-temperature case, reproduce the results reported in Ref. [33]. In conclusion, we believe that methods developed in this work will enable us to understand the goodness of convergence of the global optimization heuristics, even in cases of multi-material and possibly nano-layered coating design.

Author Contributions: Formal analysis and Supervision, V.P.; Writing—review and editing, V.G., L.T. and V.P. All authors have read and agreed to the published version of the manuscript.

Funding: This research received no external funding.

Institutional Review Board Statement: Not applicable.

Informed Consent Statement: Not applicable.

Acknowledgments: The authors are grateful for the discussion and suggestions received from the colleagues of the INFN Virgo Sannio/Salerno Group, the Virgo Coating R&D Group, and the Optics Working Group of the LIGO Scientific Collaboration.

Conflicts of Interest: The authors declare no conflict of interest.

References

1. Available online: http://www.virgo.infn.it (accessed on 27 June 2022).
2. Bersanetti, D.; Patricelli, B.; Piccinni, O. J.; Piergiovanni, F.; Salemi, F.; Sequino, V. Advanced Virgo: Status of the Detector, Latest Results and Future Prospects. *Universe* **2021**, *7*, 322. [CrossRef]
3. Available online: http://www.et-gw.eu/ (accessed on 27 June 2022).
4. Punturo, M.; Abernathy, M.; Acernese, F.; Allen, B.; Andersson, N.; Arun, K.; Barone, F.; Barr, B.; Barsuglia, M.; Beker, M.; et al. The Einstein Telescope: A third-generation gravitational wave observatory. *Class. Quant. Gravity* **2010**, *27*, 194002. [CrossRef]
5. Available online: http://www.ligo.caltech.edu (accessed on 27 June 2022).
6. Cahillane, C.; Mansell, G. Review of the Advanced LIGO Gravitational Wave Observatories Leading to Observing Run Four. *Galaxies* **2022**, *10*, 36. [CrossRef]
7. Akutsu, T.; KAGRA Scientific Collaboration. Overview of KAGRA: Calibration, detector characterization, physical environmental monitors, and the geophysics interferometer. *Prog. Theor. Exp. Phys.* **2021**, *5*, 05A102. [CrossRef]
8. Creighton, J.D.; Anderson, W.G. *Gravitational Wave Physics and Astronomy*; John Wiley and Sons: Hoboken, NJ, USA, 2011; ISBN 978-3-527-40886-3.
9. Saulson, P. *Fundamentals of Interferometric Gravitational Wave Detectors*; World Scientific: Singapore, 2017; ISBN 978-9813143074.
10. Abbott, B.P.; LIGO Scientific Collaboration; Virgo Collaboration. Observation of Gravitational Waves from a Binary Black Hole Merger. *Phys. Rev. Lett.* **2016**, *116*, 061102. [CrossRef] [PubMed]
11. Abbott, B.P.; LIGO Scientific Collaboration; Virgo Collaboration. GW170814: A Three-Detector Observation of Gravitational Waves from a Binary Black Hole Coalescence. *Phys. Rev. Lett.* **2017**, *119*, 141101. [CrossRef] [PubMed]
12. Abbott, B.P. Multi-messenger Observations of a Binary Neutron Star Merger. *Appl. J. Lett.* **2017**, *848*, L12. [CrossRef]

13. Branchesi, M. Multi-messenger astronomy: Gravitational waves, neutrinos, photons, and cosmic rays. *J. Phys. Conf. Ser.* **2016**, *718*, 022004. [CrossRef]
14. LIGO; Virgo; KAGRA Collaborations. GWTC-3: Compact Binary Coalescences Observed by LIGO and Virgo during the Second Part of the Third Observing Run. Available online: https://doi.org/10.48550/arXiv.2111.03606 (accessed on 27 June 2022).
15. Accadia T. Virgo: A laser interferometer to detect gravitational waves. *J. Instrum.* **2012**, *7*, P03012. [CrossRef]
16. Aasi, J.; LIGO Scientific Collaboration; Virgo Collaboration. Advanced LIGO. *Class. Quant. Gravity* **2015**, *32*, 074001.
17. Abernathy, M.R.; Lium, X.; Metcalf, T.H. An overview of research into low internal friction optical coatings by the gravitational wave detection community. *Mater. Res.* **2018**, *21*, e20170864. [CrossRef]
18. Flaminio, R.; Franc, J.; Michel, C.; Morgado, N.; Pinard, L.; Sassolas, B. A study of coating mechanical and optical losses in view of reducing mirror thermal noise in gravitational wave detectors. *Class. Quantum Gravity*, **2010**, *27*, 084030. [CrossRef]
19. Snyman, J.A.; Wilke, D.N. *Practical Mathematical Optimization: Basic Optimization Theory and Gradient-Based Algorithms*, 2nd ed.; Springer: Berlin/Heidelberg, Germany, 2018; ISBN 978-3-319-77585-2.
20. Pierro, V.; Fiumara, V.; Chiadini, F. Optimal Design of Coatings for Mirrors of Gravitational Wave Detectors: Analytic Turbo Solution via Herpin Equivalent Layers. *Appl. Sci.* **2021**, 11, 11669. [CrossRef]
21. Steinlechner, J.; Martin, I.W.; Hough, J.; Kruger, C.; Rowan, S.; Schnabel, R. Thermal noise reduction and absorption optimization via multimaterial coatings. *Phys. Rev. D* **2015**, *91*, 042001. [CrossRef]
22. Pierro, V.; Fiumara, V.; Chiadini, F.; Granata, V.; Durante, O.; Neilson, J.; Di Giorgio, C.; Fittipaldi, R.; Carapella, G.; Bobba, F.; et al. Ternary quarter wavelength coatings for gravitational wave detector mirrors: Design optimization via exhaustive search. *Phys. Rev. Res.* **2021**, *3*, 023172. [CrossRef]
23. Pan, H.W.; Wang, S.J.; Kuo, L.C.; Chao, S.; Principe, M.; Pinto, I.M.; DeSalvo, R. Thickness-dependent crystallization on thermal anneal for Titania/Silica nm-layer composites deposited by ion beam sputter method. *Opt. Express* **2014**, *22*, 29847. [CrossRef]
24. Durante, O.; Di Giorgio, C.; Granata, V.; Neilson, J.; Fittipaldi, R.; Vecchione, A.; Carapella, G.; Chiadini, F.; DeSalvo, R.; Dinelli, F.; et al. Emergence and Evolution of Crystallization in TiO_2 Thin Films: A Structural and Morphological Study. *Nanomaterials* **2021**, *11*, 1409. [CrossRef]
25. Abelès, F. La théorie générale des couches minces. *J. Phys. Radium* **1950**, *11*, 307–310. [CrossRef]
26. Born, M.; Wolf, E. *Principles of Optics*; Cambridge University Press: Cambridge , UK, 1997; ISBN 9780521639217.
27. Orfanidis, S.J. Electromagnetic Waves and Antennas. Available online: https://www.ece.rutgers.edu/~orfanidi/ewa/ (accessed on 27 June 2022).
28. Harry, G.; Bodiya, T.P.; De Salvo, R. *Optical Coatings and Thermal Noise in Precision Measurements*, 1st ed.; Cambridge University Press: Cambridge, UK, 2012; ISBN 9780511762314.
29. Schroeter, A.; Nawrodt, R.; Schnabel, R.; Reid, S.; Martin, I.; Rowan, S.; Schwarz, C.; Koettig, T.; Neubert, R.; Thürk, M.; et al. On the Mechanical Quality Factors of Cryogenic Test Masses from Fused Silica and Crystalline Quartz. Available online: https://arxiv.org/abs/0709.4359 (accessed on 27 June 2022).
30. Hong, T.; Yang, H.; Gustafson, E.K.; Adhikari, R.X.; Chen, Y. Brownian Thermal Noise in Multilayer Coated Mirrors. *Phys. Rev. D* **2013**, *87*, 082001. [CrossRef]
31. Vajente, G.; Yang, L.; Davenport, A.; Fazio, M.; Ananyeva, A.; Zhang, L.; Billingsley, G.; Prasai, K.; Markosyan, A.; Bassiri, R.; et al. Low Mechanical Loss TiO_2:GeO_2 Coatings for Reduced Thermal Noise in Gravitational Wave Interferometers. *Phys. Rev. Lett.* **2021**, *127*, 071101. [CrossRef]
32. Agresti, J.; Castaldi, G.; De Salvo, R.; Galdi, V.; Pierro, V.; Pinto, I.M. Optimized multilayer dielectric mirror coatings for gravitational wave interferometers. *Proc. SPIE* **2006**, *6286*, 628608.
33. Pierro, V.; Fiumara, V.; Chiadini, F.; Bobba, F.; Carapella, G.; Di Giorgio, C.; Durante, O.; Fittipaldi, R.; Mejuto Villa, E.; Neilson, J.; et al. On the performance limits of coatings for gravitational wave detectors made of alternating layers of two materials. *Opt. Mater.* **2019**, *96*, 109269. [CrossRef]
34. Deb, K. *Multi-Objective Optimization Using Evolutionary Algorithms*; John Wiley and Sons: Hoboken, NJ, USA, 2001.
35. Deb, K.; Pratap, A.; Meyarivan, T. A Fast and Elitist Multiobjective Genetic Algorithm: NSGA-II. *IEEE Trans. Evol. Comput.* **2002**, *6*, 182–197. [CrossRef]
36. Deb, K.; Jain, H. An evolutionary manyobjective optimiszation algorithm using reference-point based non-dominated sorting approach, part I: Solving problems with box constraints. *IEEE Trans. Evol. Comput.* **2014**, *18*, 577–601. [CrossRef]
37. Kukkonen, S.; Lampinen, J. GDE3: The third evolution step of generalized differential evolution. *IEEE Congr. Evol. Comput.* **2005**, *1*, 443–450.
38. Price, K.; Storn, R.M.; Lampinen, J.A. *Differential Evolution: A Practical Approach to Global Optimization*; Springer: Berlin/Heidelberg, Germany, 2005; ISBN 978-3-540-20950-8.
39. Zhang, Q.; Li, H. MOEA/D: A multiobjective evolutionary algorithm based on decomposition. *IEEE Trans. Evol. Comput.* **2007**, *11*, 712–731. [CrossRef]
40. Fan, Z.; Fang, Y.; Li, W.; Cai, X.; Wei, C.; Goodman, E. MOEA/D with angle-based constrained dominance principle for constrained multi-objective optimization problems. *Appl. Soft Comput.* **2019**, *74*, 621–633. [CrossRef]
41. Holland, J.H. *Adaptation in Natural and Artificial Systems*; University of Michigan Press: Ann Arbor, MI, USA, 1975.
42. Hadka, D.; Reed, P.M. Borg: An Auto-Adaptive Many-Objective Evolutionary Computing Framework. *Evol. Comput.* **2013**, *21*, 231–259. [CrossRef] [PubMed]

43. Feldt, R. BlackBoxOptim, GitHub Repository. Available online https://github.com/robertfeldt/BlackBoxOptim.jl (accessed on 27 June 2022).
44. Kennedy, J.; Eberhart, R. Particle Swarm Optimization. In Proceedings of the IEEE International Conference on Neural Networks IV, Perth, WA, Australia, 27 November–1 December 1995; pp. 1942–1948.
45. Shi, Y.; Eberhart, R.C. A modified particle swarm optimizer. In Proceedings of the IEEE International Conference on Evolutionary Computation, Anchorage, AK, USA, 4–9 May 1998; pp. 69–73.
46. Bonyadi, M.R.; Michalewicz, Z. Particle swarm optimization for single objective continuous space problems: A review. *Evol. Comput.* **2017**, *25*, 1–54. [CrossRef]
47. GitHub Repository. Available online: https://github.com/Project-Platypus/Platypus (accessed on 27 June 2022).
48. GitHub Repository. Available online: https://github.com/jMetal/jMetal (accessed on 27 June 2022).
49. Mishra, K.K.; Harit, S. A Fast Algorithm for Finding the Non Dominated Set in Multi objective Optimization. *Int. J. Comput. Appl.* **2010**, *1*, 35–39.
50. Coello Coello, C.A. Evolutionary multi-objective optimization: A historical view of the field. *IEEE Comput. Intell. Mag.* **2006**, *1*, 28–36. [CrossRef]
51. Gaudrie, D.; le Riche, R.; Picheny, V.; Enaux, B.; Herbert, V. Budgeted Multi-Objective Optimization with a Focus on the Central Part of the Pareto Front. Available online: https://arxiv.org/abs/1809.10482 (accessed on 27 June 2022).
52. Agresti, J.; Castaldi, G.; De Salvo, R.; Galdi, V.; Pierro, V.; Pinto, I. M. Optimized Coatings. LIGO Document, 2005, G050363. Available online: https://dcc.ligo.org/LIGO-G050363/public (accessed on 27 June 2022).